Dalton Transactions

Accepted Manuscript

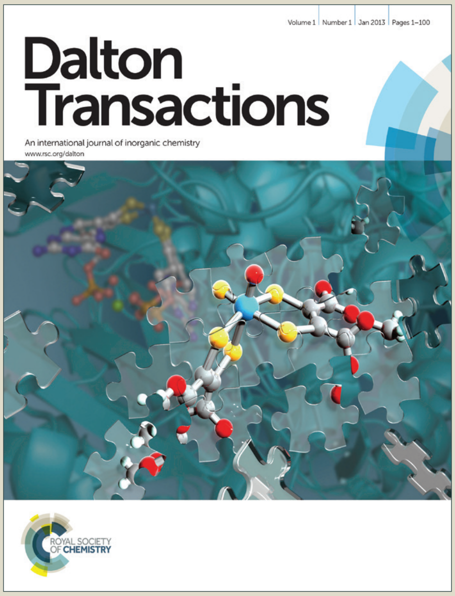

ROYAL SOCIETY OF CHEMISTRY

www.rsc.org/dalton

Synthesis of g-C_3N_4/$CaIn_2S_4$ composites with enhanced photocatalytic activity under visible light irradiation

Wenhui Yuan[a*] Sai Yang[a] Li Li[b]

A series of Graphite-like g-C_3N_4 hybridized $CaIn_2S_4$ photocatalysts with different g-C_3N_4 content were fabricated via a facile hydrothermal synthetic method. These as-prepared samples were characterized by X-ray diffraction (XRD), scanning electron microscopy (SEM), transmission electron microscopy (TEM), UV-Visible absorption spectra (UV-Vis) and Fourier transform infrared (FT-IR) spectra. Under visible light irradiation, the as-prepared g-C_3N_4/$CaIn_2S_4$ nanocomposites showed enhanced photocatalytic performance for rhodamine B (RhB) degradation. The sample with 5 wt% g-C_3N_4 hybridized $CaIn_2S_4$ exhibited the highest photocatalytic activity. The enhanced photocatalytic performance under visible light irradiation could be attributed to the high separation efficiency of the photogenerated electron-hole pairs. This work could provide a new insight into the fabrication of visible light driven photocatalysts with efficient and stable performance.

Keywords: $CaIn_2S_4$, g-C_3N_4, nanocomposites, visible-light photocatalysis

Introduction

. In past decades, photocatalysis has attracted a lot of attention because of its potential application in the field of energy conversion and pollutant degradation. Various researches have focused on exploiting novel and more efficient photocatalysts for degradation of organic contaminants in wastewater [1]. The

---

[*] Corresponding author. Tel: +86 20 8711 1887; fax: +86 20 8711 1887. E-mail address: cewhyuan@scut.edu.cn
Present Address: School of Chemistry and Chemical Engineering, South China University of Technology, Wushan, Tianhe, Guangzhou 510640, P. R. China.

semiconductor photocatalysis technique has been regarded as a promising approach to address the increasing global energy and environmental crises [2]. Given the characteristic of low energy consumption and green, semiconductor photocatalysts are regarded as the environmental-friendly technologies for degradation of organic dyes [3-6]. What really matters in the photocatalytic degradation of dye molecules pollutant is how to design photocatalyst with high degradation efficiency [7]. A class of ‘multi metal component’ oxide semiconductors which is gaining attention from scientific community is ‘AIn_2S_4’ type metal sulfides. Most metal sulfides are promising candidates for visible-light-driven photocatalysts because of their narrow band gaps and band edge levels at relatively negative potentials compared to oxides [8], such as $ZnIn_2S_4$ [9-11], $CdIn_2S_4$ [12-13]. $CaIn_2S_4$ is a ternary semiconductor chalcogenide that belongs to the AB_2X_4 family of ternary compounds. Recent study found that ternary $CaIn_2S_4$, first synthesized using a facile hydrothermal method, can produce hydrogen from pure water without any cocatalysts under visible light irradiation [14]. However, the low separation efficiency of photogenerated charge carriers has limited their large-scale practical application. Among various strategies, the rapid separation-transfer-transformation of photo-generated charge carriers is a key issue which should be addressed [15]. One of the techniques for increasing the separation efficiency of photogenerated electron-hole pairs is to form a composite photocatalyst using two kinds of semiconductors [16]. Composite photocatalysts as the separation efficiency of photogenerated charge carriers with two or more components have attract extensive scientific interest. For example, Ding synthesized the $CaIn_2S_4$Reduced Graphene Oxide Nanocomposites for efficient RhB degradation under visible light irradiation [17]. Very recently, considerable interest has been focus on graphite-like carbon nitride (g-C_3N_4) with a direct band gap and typical two dimensional (2D) nanostructure, which exhibits a high visible light photocatalytic performance for the degradation of organic pollutants [18-20]. This material would be a promising photocatalyst owing to its absorption of visible light, low price, and high stability, along with its unique chemical and catalytic properties [21]. Up to now, several kinds of C_3N_4 based heterojunctions have been developed, such as g-C_3N_4/Bi_2WO_6 [22-23], g-C_3N_4/$ZnWO_4$ [24] and g-C_3N_4/Ag_3VO_4 [25], g-C_3N_4/Ag_3PO_4 [26], g-C_3N_4/Co_3O_4 [27], g-C_3N_4/$CuInS_2$ [28]. The key link of constructing a heterojunction is to seek narrow band gap semiconductors with well-matched band-structure [29]. Considering the previous research, g-C_3N_4 is chosen to modify $CaIn_2S_4$ to form the new composites. The combination of g-C_3N_4 and $CaIn_2S_4$ can be an ideal system to extend the absorption to visible light and at the same time to achieve a high separation efficiency of photogenerated electron-hole pairs. To the best of our knowledge, the effect of g-C_3N_4 on the photocatalytic performance of $CaIn_2S_4$ has not been reported. Herein, we present a new example of g-C_3N_4 hybridized $CaIn_2S_4$ photocatalyst. The synergistic effect between $CaIn_2S_4$ and g-C_3N_4 and the possible mechanisms of enhancement of photocatalytic activity were systematically investigated.

Experimental

Preparation of samples

All of the chemical reagents were of analytical grade and used without further purification. The water used was deionized. The g-C_3N_4 powders were prepared according to the literature [30]. The metal-free g-C_3N_4 powders were synthesized by heating melamine in muffle furnace at different temperatures. In a typical synthesis run, 5 g melamine was placed into an alumina crucible with a cover. Then the crucible was heated up to 550 °C and held for 2 h with a heating rate of 10 °C/min. Further deamination treatment was performed at 550°C for 2 h. The resulting yellow product was collected, and ground into powder for further use. The typical preparation of g-C_3N_4/$CaIn_2S_4$ photocatalysts was as follows: an appropriate amount of C_3N_4 was completely dispersed in 60 mL deionized water assisted by ultrasonication. In detail, 1.18 g Ca $(NO_3)_2 \cdot 4H_2O$ (5 mmol), 3.0 g In $(NO_3)_3$ (10 mmol), and 3.0 g CH_3CSNH_2 (40 mmol, double amount) were added into the suspension. The mixture was stirred for 30 min and then transferred to a 200 mL Teflon-lined stainless steel autoclave. A hydrothermal reaction took place in the sealed autoclave at 160 °C for 16 h. Then, the autoclave was removed from oven and allowed to cool in air. Yellow precipitates were obtained by decantation followed by washing with distilled water and ethanol for several times. The product was then dried at 80 °C for 6 h. According to this method, different weight ratios of g-C_3N_4/$CaIn_2S_4$ from 1 wt% to 10 wt% were synthesized. The composite catalysts were labeled as x-g-C_3N_4/$CaIn_2S_4$, and x presented the g-C_3N_4 loading amount (1 wt%, 3 wt%, 5 wt%, 8 wt% and 10 wt%).

Characterization of materials

X-ray diffraction (XRD) patterns were obtained by Bruker D8 Advance X-ray diffractometer with Cu-Kα irradiation (λ = 1.54 Å) at 40 kV and 40 mA. The general morphology of the products was examined by scanning electron microscopy (SEM) on a JEOL JSM 6700F instrument operated at 20 kV. The transmission electron microscopy (TEM) images were measured by JEOL model JEM 2100 EX instrument at the accelerating voltage of 200 kV. The specific surface area and porosity of the samples were measured by N_2 adsorption at 77K on a Micrometritics ASAP2020 analyzer and calculate by the Brunauer-Emmett-Teller (BET) method. Fourier transform infrared (FT-IR) spectra were recorded on a Nicolet Avatar 370 spectrophotometer using the standard KBr disk method. All of the samples were degassed at 120 °C overnight prior to BET measurements. The UV-Vis diffuse reflectance spectra (DRS) were conducted with a Varian Cary 500 UV-Vis spectrophotometer with $BaSO_4$ as the reference.

Photocatalytic activity measurement

The photocatalytic activities of all powders were evaluated by degradation of RhB aqueous solution. The visible light was obtained by a 250 W tungsten-halogen lamp with a 420 nm cut off filter. A suspension containing 100 mg of catalyst and a fresh RhB aqueous solution (120 mL, 30 mg/L) was magnetically stirred in the dark for 30 min to establish an adsorption/desorption equilibrium. At certain time intervals, 3~4 mL of suspension was sampled and the particles were removed. The filtrate was analyzed by a UV-Vis spectrophotometer (UV-2450) and the absorption peaks at maximum absorption wavelength for RhB were monitored.

Results and discussion

Phase structure

Fig.1 shows the XRD patterns of $CaIn_2S_4$ and g-C_3N_4/$CaIn_2S_4$ composites. In general, no obvious difference in XRD patterns was observed among all the samples. The main diffraction peaks of all the samples at 27.4°, 28.4°, 33.1°, 43.4°, and 47.7°, correspond to the diffractions of the (311), (222), (400), (511), and (440) planes of $CaIn_2S_4$ (PCPDF #310272), respectively. No other impurity peaks corresponding to binary sulfides or oxides related to the reactants are detected, indicating the pure phase of $CaIn_2S_4$. For pure g-C_3N_4 sample, the characteristic peaks at 27.3° and 12.9°

correspond to the (002) plane arising from the stacking of the conjugated aromatic system, and the (100) plane diffraction arising from the in-plane repeating motifs of the continuous heptazine network, respectively [31]. As coupling these two semiconductors, in g-C_3N_4/$CaIn_2S_4$ heterojunction samples similar diffractions to the pure $CaIn_2S_4$ are observed, indicating that the heterogeneous process would not bring any influence on the crystal structure. Furthermore, there is not any characteristic diffraction peaks for g-C_3N_4 observed in the XRD patterns even though the content of g-C_3N_4 is as high as 10 wt%, mainly due to its relatively low diffraction intensity and high dispersion [32-33]. Similar results are also observed in some other C_3N_4 based heterojunctions, such as C_3N_4-$ZnWO_4$ and C_3N_4-Bi_2WO_6 [24, 29, 34].

Morphological structure

Fig. 2 shows the SEM images of $CaIn_2S_4$ and g-C_3N_4/$CaIn_2S_4$ photocatalysts. The pure $CaIn_2S_4$ samples appeared to be aggregated particles, which contained many smaller irregular $CaIn_2S_4$ crystals, as shown in Fig. 2a. From Fig. 2(b), the pure g-C_3N_4 displays aggregated morphologies, which are comprised of block-based flakiness and particles. However, the g-C_3N_4/$CaIn_2S_4$ composites showed agglomeration structures, which were similar to pure $CaIn_2S_4$. As shown in Fig. 2c~g, amounts of $CaIn_2S_4$ particles are deposited on the surface of g-C_3N_4, resulting in the formation of a heterostructure. In addition, the density of $CaIn_2S_4$ particles deposited on the g-C_3N_4 surface increases step-by-step with the increase of g-C_3N_4 content. In the case of 5 wt% g-C_3N_4/$CaIn_2S_4$ heterojunction, the surface of g-C_3N_4 has been covered by $CaIn_2S_4$ particles well. However, further increase of g-C_3N_4 content results in a drastic overlapping of $CaIn_2S_4$ particles, which is helpless for fabrication of heterojunction with a close interface. This result confirmed the formation of heterojunction between g-C_3N_4 and $CaIn_2S_4$ through the hydrothermal process and showed the intimate contact between g-C_3N_4 and $CaIn_2S_4$.

The morphology and the dispersion state of $CaIn_2S_4$ and 5 wt% g-C_3N_4/$CaIn_2S_4$ composite were analyzed by TEM and shown in Fig. 3. Fig. 3a is the morphology image of pure $CaIn_2S_4$, it can be seen that $CaIn_2S_4$ are granular like. The pure g-C_3N_4 owns a typically layered structure, and its surface is relatively smooth and flat, as shown in Fig. 3b. Fig. 3c is the morphology image of 5 wt% g-C_3N_4/$CaIn_2S_4$ composite. Before the TEM analysis, a typical preparation procedure was proposed by ultrasonic processing the as-prepared samples for 30 min. Even so, the $CaIn_2S_4$ did not peel off from the g-C_3N_4, which implies that the interaction between $CaIn_2S_4$ and g-C_3N_4 is very strong. It is suggested that a heterojunctions structure was formed, which is beneficial for electrons transfer between component semiconductors [35]. This tight coupling is favorable for the charge transfer between g-C_3N_4 and $CaIn_2S_4$ and promotes the separation of photogenerated electron-hole pairs, subsequently improving the photocatalytic activity. Moreover, this result also suggests that the g-C_3N_4/$CaIn_2S_4$ heterojunctions in structure are heterogeneous rather than a physical mixture of two separate phases of g-C_3N_4 and $CaIn_2S_4$.

FT-IR characterization

The composition of g-C_3N_4/$CaIn_2S_4$ heterojunctions was further characterized by FT-IR spectroscopy, as shown in Fig. 4. It can be clearly seen that the main characteristic peaks of pure g-C_3N_4 sample. In the spectrum of g-C_3N_4 , the strong peaks at 3420 cm^{-1} and 3200 cm^{-1} could be ascribed to the absorbed water molecules and stretching mode of N-H resulted from incomplete condensation [36-37], respectively. The absorbance peak at about 810 cm^{-1} was originated from the characteristic breathing mode of s-triazine, and the peaks at 1000-1750 cm^{-1} region were associated with either C-N or C=N stretching mode [38-40]. Naturally, all absorption bands of g-C_3N_4 also still present in g-C_3N_4/$CaIn_2S_4$ heterojunctions, obviously demonstrating that these heterojunctions contain two fundamental components: g-C_3N_4 and $CaIn_2S_4$.

Optical properties

It is known that the optical absorption of a semiconductor is closely related to its electronic structure [41]. The UV-vis diffuse reflectance spectra of g-C_3N_4, $CaIn_2S_4$ and g-C_3N_4/$CaIn_2S_4$ composites are shown in Fig. 5. Pure $CaIn_2S_4$ shows a wide absorption in visible region with an absorption edge end at about 575 nm. Meanwhile, g-C_3N_4 has an absorption edge at 470 nm. The band gap values were determined to be about 2.9 eV for g-C_3N_4 and 1.96 eV for $CaIn_2S_4$ according to the Tauc equation. g-C_3N_4/$CaIn_2S_4$ composites had only one absorption inflection point and kept the same absorption edge with $CaIn_2S_4$ at about 575 nm. The same absorption edge indicated that the band gap of $CaIn_2S_4$ was unchanged. Compared with pure $CaIn_2S_4$, all the hybrid composites show slight absorption red-shift, which indicates that the visible light response of these samples have been successfully extended by the hybridization with g-C_3N_4. However, it should be point out that the visible light absorption ability of hybrid samples does not significantly increase with increasing amount of g-C_3N_4. As g-C_3N_4 content was increased from 1 wt% to 5 wt%, an enhanced absorption in visible region from 575 nm to 800 nm was observed for g-C_3N_4/$CaIn_2S_4$ composites. The absorbance increased with the increase of the amount of g-C_3N_4. Such an additional broad band ($\lambda > 575$ nm) could be attributed to the absorption of g-C_3N_4 phase and revealed the increase of the loading amount of g-C_3N_4

on the surface of $CaIn_2S_4$. Furthermore, the intimate contact between g-C_3N_4 and $CaIn_2S_4$ might also contribute to the greater absorption.

BET Specific Surface Area Analyses

The nitrogen adsorption-desorption isotherms of $CaIn_2S_4$ and g-C_3N_4/$CaIn_2S_4$ composites are presented in Fig. 6. Obviously, all the samples exhibit type IV isotherms with type H_3 hysteresis loop according to the IUPAC classification, indicating that the samples have a mesoporous structure [42-44]. The BET specific surface area and pore volume of g-C_3N_4/$CaIn_2S_4$ increases with the increase in the content of g-C_3N_4 up to 5 wt%. The BET specific surface area of 5 wt% g-C_3N_4/$CaIn_2S_4$ was much larger than that of pure $CaIn_2S_4$, suggesting that the opposite amount of g-C_3N_4 could significantly increase the specific surface area of the final product. When the content of g-C_3N_4 is higher than 5 wt%, the BET specific surface area and pore volume of the samples are decreased, as listed in Table 1. Therefore, the incorporation of g-C_3N_4 has an obvious effect on the pore structure and specific surface area of g-C_3N_4/$CaIn_2S_4$ photocatalysts. As we know, larger specific surface area will provide more adsorptive/active sites during the photocatalytic reaction, which can be beneficial for the improvement of the photocatalytic activity.

Photocatalytic activity and the stability of the catalysts

The photocatalytic performance of all samples was evaluated by degradation of RhB solution under visible light irradiation and the fixed irradiation time was 60 min, as shown in Fig. 7. According to the literature, RhB had only about 5% self-degradation after irradiation for 60 min, which means the self-degradation effect of RhB was almost negligible under visible light irradiation [17]. Before light was turned on, the suspensions were magnetically stirred in the dark for 30 min to ensure absorption-desorption equilibrium between the photocatalyst and RhB. In the meantime, the as-prepared different ratios of composites exhibited markedly higher photocatalytic activity than that of pure $CaIn_2S_4$ under visible light irradiation. For the hybrid photocatalysts, the photocatalytic activity was related to g-C_3N_4 content of the composites. With the increase of g-C_3N_4 content from 1 to 5 wt%, the degradation rate of RhB was increased gradually from 91% to 96.3%. However, further increasing the g-C_3N_4 content to 8 wt% or 10 wt%, the photocatalytic ability of g-C_3N_4/$CaIn_2S_4$ composites presents decreasing trend. Under the experimental conditions, the optimum amount of g-C_3N_4 in the g-C_3N_4/$CaIn_2S_4$ composites is 5 wt%. This result proves that these changes in the photocatalytic activity could be understood through considering the synergetic effects of light absorption and heterojunction structure of g-C_3N_4/$CaIn_2S_4$. The reason that excessive g-C_3N_4 in g-C_3N_4/$CaIn_2S_4$ composite decreased the photodegradation property could be concluded as follows: the joint effect between the excellent charge transfer capability of g-C_3N_4 and its detrimental effect on visible light absorption and the high content of g-C_3N_4 could significantly affect the particle size and distribution of $CaIn_2S_4$ nanoparticles due to the serious agglomeration, which was confirmed by SEM images. This fact indicated that the heterojunction between g-C_3N_4 and $CaIn_2S_4$ was indispensable for the electron transfer between the two components and was the key factor for the enhancement of photocatalytic activity.

The stability of photocatalysts is important for its assessment and application [45]. The 5 wt% g-C_3N_4/$CaIn_2S_4$ photocatalyst was selected as a sample to ascertain the stability. In the cyclic experiment, the recovered photocatalyst was centrifuged and dried at 80 ◦C for 2 h. The repetition tests reveal that there is no obvious decrease in the photocatalytic efficiency of RhB after five times experiments, which indicates that 5 wt% g-C_3N_4/$CaIn_2S_4$ has a good stability in the photocatalytic reaction process. The stability of 5 wt% g-C_3N_4/$CaIn_2S_4$ was also investigated by XRD patterns of the fresh and used samples. As shown in Fig. 8b, the XRD patterns of the fresh and used samples have no obvious change.

Mechanisms of photocatalysis

According to the analyses above, the excellent visible-light photocatalytic activity of g-C_3N_4/$CaIn_2S_4$ composites could be attributed to the synergetic effects and charge transfer between $CaIn_2S_4$ and g-C_3N_4. For the photocatalytic process, the efficient charge separation and transfer are crucial for the photocatalytic activity [46]. Fig. 9 shows the energy level positions of the bands of g-C_3N_4 and $CaIn_2S_4$. When $CaIn_2S_4$ was loaded on the surface of g-C_3N_4 with hydrothermal process, heterojunction between g-C_3N_4 and $CaIn_2S_4$ was formed, which was proved by FT-IR, SEM and TEM results. The heterojunction was a key factor for the enhancement of photocatalytic activity. For heterojunctions, when the band positions of the material were appropriate, electron transfer could be realized [47]. Under the excitation of visible light, photo-induced electrons and holes were produced in the conduction band and valance band of $CaIn_2S_4$, respectively. As showed in Fig. 9, on the interface where heterojunction formed, the photo-induced electrons produced in $CaIn_2S_4$ conduction band transferred to g-C_3N_4 conduction band. When photo-induced electrons generated by $CaIn_2S_4$ remained the same and transferred to g-C_3N_4, the recombination possibility of electron-hole pairs decreased. Furthermore, the heterojunction can efficiently separate the photo-induced electron-hole pairs and prevent the recombination. There were three ways to consume photo-induced electrons [48]: (a) recombine with holes inside the material (volume recombination); (b) recombine with spices on particle surface (surface recombination); (c) react with

O_2 to produce $\cdot O_2^-$. As a result, the separation efficiency of photogenerated charge carriers can be effectively improved at the interface of the nanocomposites. Obviously, the improved photocatalytic efficiency of the g-C_3N_4/$CaIn_2S_4$ photocatalysts can be attributed to the synergistic effect of the two components. Such special heterstructure composite composed of apposite proportion is assumed to be beneficial for photogenerated charge separation and therefore lead to enhanced photocatalytic activity. Moreover, the shift of the binding energy also indicated that through the hydrothermal synthesis process, an intimate contact was formed between g-C_3N_4 and $CaIn_2S_4$ through the hydrothermal synthesis process, which is consistent with the TEM results.

Conclusion

g-C_3N_4/$CaIn_2S_4$ composites with different g-C_3N_4 content were successfully prepared and characterized. The as-prepared g-C_3N_4/$CaIn_2S_4$ had strong absorption in the visible light region with the optical band gap of the composites unchanged. The BET specific surface areas of g-C_3N_4/$CaIn_2S_4$ composites were larger than that of pure $CaIn_2S_4$. Under visible light irradiation, the RhB photodegradation by the g-C_3N_4/$CaIn_2S_4$ composites was greater than that for $CaIn_2S_4$ alone. The photocatalytic results indicated that the highest RhB degradation of 96.3% was achieved on the 5 wt% g-C_3N_4/$CaIn_2S_4$ sample. When the content of g-C_3N_4 is higher than 5 wt%, the RhB photodegradation by the g-C_3N_4/$CaIn_2S_4$ composites were decreased. The photocatalytic activity of the composite can be ascribed to the heterojunctions between g-C_3N_4 and $CaIn_2S_4$, which facilitate the separation of photogenerated electrons and holes. The photodegradation mechanism was proposed and discussed in terms of energy band positions. The present g-C_3N_4/$CaIn_2S_4$ composite is thought to be a very effective visible-light-driven photocatalyst and could be used to remove organic pollutants from industrial waste water.

Acknowledgments

The authors gratefully acknowledge the financial support of National Natural Science Foundation of China (No.20976057) and research fund of The Guangdong Provincial Engineering Research Centre of Green Fine Chemicals, China.

Notes and references

[a]*School of Chemistry and Chemical Engineering, South China University of Technology, Guangdong Guangzhou 510640; Tel: +86 20 8711 1887; fax: +86 20 8711 1887. E-mail address: cewhyuan@scut.edu.cn; Present Address: School of Chemistry and Chemical Engineering, South China University of Technology, Wushan, Tianhe, Guangzhou 510640, P. R. China.*

[b]*School of Environment Energy, South China University of Technology, Guangdong Guangzhou 510006*

Electronic Supplementary Information (ESI) available: **Figure SI 1.** XRD patterns of $CaIn_2S_4$, g-C_3N_4 and g-C_3N_4/$CaIn_2S_4$ composites with variation of g-C_3N_4 content (a) 0, (b) 1 wt%, (c) 3 wt%, (d) 5 wt%, (e) 8 wt%, (f) 10 wt%. **Figure SI 2.** SEM images of the g-C_3N_4/$CaIn_2S_4$ heterojunction composites: (a) $CaIn_2S_4$; (b) pure g-C_3N_4; (c) 1 wt% g-C_3N_4/$CaIn_2S_4$; (d) 3 wt% g-C_3N_4/$CaIn_2S_4$; (e) 5 wt% g-C_3N_4/$CaIn_2S_4$; (f) 8 wt% g-C_3N_4/$CaIn_2S_4$; (g) 10 wt% g-C_3N_4/$CaIn_2S_4$. **Figure SI 3.** TEM images of (a) $CaIn_2S_4$, (b) g-C_3N_4, (c) 5 wt% g-C_3N_4/$CaIn_2S_4$. **Figure SI 4.** FT-IR spectra of $CaIn_2S_4$, g-C_3N_4 and g-C_3N_4/$CaIn_2S_4$ composites. **Figure SI 5.** UV-vis DRS spectra of $CaIn_2S_4$, g-C_3N_4 and g-C_3N_4/$CaIn_2S_4$ composites. **Figure SI 6.** Nitrogen adsorption-desorption isotherms of g-C_3N_4/$CaIn_2S_4$ composites. **Figure SI 7.** Concentration change of RhB as the function of the irradiation time. **Figure SI 8.** (a) Cycling runs for the photocatalytic degradation of RhB over 5 wt% g-C_3N_4/$CaIn_2S_4$ sample under visible light irradiation; (b) XRD patterns of the 5 wt% g-C_3N_4/$CaIn_2S_4$ sample before and after the cycling photocatalytic experiments. **Figure SI 9.** Energy band diagram and photocatalytic mechanism of g-C_3N_4/$CaIn_2S_4$ composites. **Table 1** Surface area, pore volume over g-C_3N_4/$CaIn_2S_4$ photocatalysts

[1] H. Xu, H.M. Li, C.D. Wu, J.Y. Chu, Y.S. Yan, H.M. Shu, Z. Gu, J. Hazard. Mater. , 2008, **153**, 877-884.

[2] R. Shi, J. Lin, Y.J. Wang, J. Xu, Y.F. Zhu, J. Phys. Chem. C, 2010, **114**, 6472-6477.

[3] Y. Tian, B. Chang, Z. Yang, B. Zhou, F. Xi, X. Dong, RSC Adv., 2014, **4**, 4187-4193.

[4] M.S.A.S. Shah, A.R. Park, K. Zhang, J.H. Park, P.J. Yoo, ACS Appl. Mater. Interfaces, 2012, **4**, 3893-3901.

[5] S. Cao, K.L. Yeung, P.L. Yue, Appl. Catal. B: Environ., 2006, **68**, 99-108.

[6] Z. Li, S. Yang, J. Zhou, D. Li, X. Zhou, C. Ge, Y. Fang, Chem. Eng. J., 2014, **241**, 344-351.

[7] X.T. Wu, C.G. Liu, X.F. Li, X.G. Zhang, C. Wang, Y.K. Liu, Mat. Sci. Semicon. Proc., 2015, **32**, 76-81.

[8] A. Kudo, I. Tsuji, H. Kato, Chem. Commun., 2002, **17**, 1958-1959.

[9] Y. Xie, Y.F. Liu, H.L. Cui, W. Zhao, C.Y. Yang, F.Q. Huang, J. Power Sources, 2014, **265**, 62-66.

[10] W.H. Yuan, X.C. Liu, L. Li, Acta Phys. Chim. Sin., 2013, **29**, 151-156.

[11] S. Yang, L. Li, W.H. Yuan, Z.L. Xia, Dalton Trans., 2015, **44**, 6374-6383.

[12] Y.G. Yu, G. Chen, G. Wang, Z.S. Lv, Int. J. Hydrogen Energy, 2013, **38**, 1278-1285.

[13] W.J. Wang, T. W. Ng, W. K. Ho, J.H. Huang, S.J. Liang, T.C. An, G.Y. Li, J.C. Yu, P. K. Wong, Appl. Catal. B: Environ., 2013, **129**, 482-490.

[14] J.J. Ding, S. Sun, W.H. Yan, J. Bao, C. Gao, Int. J. Hydrogen Energy, 2013, **38**, 13153-13158.

[15] C. C. Han, L.E. Wu, L. Ge, Y.J. Li, Z. Zhao, Carbon, 2015, **92**, 31-40.

[16] K. Katsumata, R. Motoyoshi, N. Matsushita, K. Okada, J. Hazard. Mater., 2013, **260**, 475-482.

[17] J.J. Ding , W.H. Yan, S. Sun, J. Bao, C. Gao, ACS Appl. Mater. Interfaces, 2014, **6**, 12877-12884.

[18] S. Yan, Z. Li, Z. Zou, Langmuir, 2009, **25**, 10397-10401.

[19] F. Dong, L. Wu, Y. Sun, M. Fu, Z. Wu, S.C. Lee, J. Mater. Chem., 2011, **21**, 15171-15174.

[20] F. Dong, Y. Sun, L. Wu, M. Fu, Z. Wu, Catal. Sci. Technol., 2012, **2**, 1332-1335.

[21] Y. Wang, X. Wang, M. Antonietti, Angew. Chem. Int. Edit., 2012, **51**, 68-89.

[22] Y. Wang, X. Bai, C. Pan, J. He, Y. Zhu, J. Mater. Chem., 2012, **22**, 11568-11573.

[23] Y. Tian, B. Chang, J. Lu, J. Fu, F. Xi, X. Dong, ACS Appl. Mater. Interfaces, 2013, **5**, 7079-7085.

[24] Y.J. Wang, Z.X. Wang, S. Muhammad, J. He, CrystEngComm, 2012, **14**, 5065-5070.

[25] T.T. Zhu, Y.H. Song, H.Y. Ji, Y.G. Xu, Y.X. Song, J.X. Xia, S. Yin, Y.P. Li, H. Xu, Q. Zhang, H.M. Li, Chem. Eng. J., 2015, **271**, 96-105.

[26] S. Kumar, T. Surendar, A. Baruah, V. Shanker, J. Mater. Chem. A, 2013, **1**, 5333-5340.

[27] C. Han, L. Ge, C. Chen, Y. Li, X. Xiao, Y. Zhang, L. Guo, Appl. Catal. B: Environ., 2014, **147**, 546-553.

[28] F. Yang, V. Kuznietsov, M. Lublow, C. Merschjann, A. Steigert, J. Klaer, A. Thomas,T. Schedel-Niedrig, J. Mater. Chem. A, 2013, **1**, 6407-6415.

[29] Y.L. Tian, B.B. Chang, J.L. Lu, J. Fu, F.G. Xi, X.P. Dong, ACS Appl. Mater. Interfaces, 2013, **5**, 7079-7085.

[30] L. Ge, Mater. Lett., 2011, **65**, 2652-2654.

[31] J.H. Sun, J.S. Zhang, M.W. Zhang, M. Antonietti, X.Z. Fu, X.C. Wang, Nat. Commun., 2012, **2**, 1139.

[32] W.G. Wang, J.G. Yu, Q.J. Xiang, B. Cheng, Appl. Catal. B: Environ., 2012, **119-120**, 109-116.

[33] J.X. Low, J.G. Yu, Q. Li, B. Cheng, Phys. Chem. Chem. Phys., 2014, **16**, 1111-1120.

[34] Y. Wang, X. Bai, C. Pan, J. He, Y. Zhu, J. Mater. Chem., 2012, **22**, 11568-11573.

[35] L.Y. Huang, H. Xu, Y.P. Li, H.M. Li, X.N. Cheng, J.X. Xia, Y.G. Xu, G.B. Cai, Dalton Trans., 2013, **42**, 8606-8616.

[36] Y.M. He, J. Cai, L.H. Zhang, X.X. Wang, H.J. Lin, B.T. Teng, L.H. Zhao, W.Z. Teng, H.L. Wan, M.H. Fan, Ind. Eng. Chem. Res., 2014, **53**, 5905-5915.

[37] C. Chang, L.Y. Zhu, S.F. Wang, X.L. Chu, L.F. Yue, ACS Appl. Mater. Interfaces, 2014, **6**, 5083-5093.

[38] Y. Cui, Z. Ding, X. Fu, X. Wang, Angew. Chem. Int. Edit., 2012, **51**, 11814-11818.

[39] H.P. Li, J.Y. Liu, W.G. Hou, N. Du, R.J. Zhang, X.T. Tao, Appl. Catal. B: Environ., 2014, **160-161**, 89-97.

[40] A. Thomas, A. Fischer, F. Goettmann, M. Antonietti, J.O. Mueller, R. Schloegl, J.M. Carlsson, J. Mater. Chem., 2008, **18**, 4893-4908.

[41] J.F. Zhang , Y.F. Hu, X.L. Jiang, S.F. Chen, S.G. Meng, X.L. Fu, J. Hazard. Mater., 2014, **280**, 713-722.

[42] L.S. Zhang, K.H. Wong, H.Y. Yip, C. Hu, J.C. Yu, C.Y. Chan, P.K. Wong, Environ. Sci. Technol., 2010, **44**, 1392-1398.

[43] X. Li, R. Huang, Y. Hu, Y. Chen, W. Liu, R. Yuan, Z. Li, Inorg. Chem., 2012, **51**, 6245-6250.

[44] P. Madhusudan, J.R. Ran, J. Zhang, J.G. Yu, G. Liu, Appl. Catal. B: Environ., 2011, **110**, 286-295.

[45] C.C. Han, L. Ge, C.F. Chen, Y.J. Li, X.L. Xiao, Y.N. Zhang, L.L. Guo, Appl. Catal. B: Environ., 2014, **147**, 546-553.

[46] L. Ge, C.C. Han, X.L. Xiao, L.L. Guo, Appl. Catal. B: Environ., 2013, **142-143**, 414-422.

[47] H. Dong, G. Chen, J. Sun, Y. Feng, C. Li, G. Xiong, C. Lv, Dalton Trans., 2014, **43**, 7282-7289.

[48] J. Xu, X.J. Cao, Chem. Eng. J., 2015, **260**, 642-648.

Figure Captions

Fig. 1. XRD patterns of $CaIn_2S_4$, g-C_3N_4 and g-C_3N_4/$CaIn_2S_4$ composites with variation of g-C_3N_4 content (a) 0, (b) 1 wt%, (c) 3 wt%, (d) 5 wt%, (e) 8 wt%, (f) 10 wt%.

Fig. 2. SEM images of the g-C_3N_4/$CaIn_2S_4$ heterojunction composites: (a) $CaIn_2S_4$; (b) pure g-C_3N_4; (c) 1 wt% g-C_3N_4/$CaIn_2S_4$; (d) 3 wt% g-C_3N_4/$CaIn_2S_4$; (e) 5 wt% g-C_3N_4/$CaIn_2S_4$; (f) 8 wt% g-C_3N_4/$CaIn_2S_4$; (g) 10 wt% g-C_3N_4/$CaIn_2S_4$.

Fig. 3. TEM images of (a) $CaIn_2S_4$, (b) g-C_3N_4, (c) 5 wt % g-C_3N_4/$CaIn_2S_4$.

Fig. 4. FT-IR spectra of $CaIn_2S_4$, g-C_3N_4 and g-C_3N_4/$CaIn_2S_4$composites.

Fig. 5. UV-vis DRS spectra of $CaIn_2S_4$, g-$C_3N_4$and g-C_3N_4/$CaIn_2S_4$ composites.

Fig. 6. Nitrogen adsorption-desorption isotherms of g-C_3N_4/$CaIn_2S_4$ composites.

Fig. 7. Concentration change of RhB as the function of the irradiation time.

Fig. 8. (a) Cycling runs for the photocatalytic degradation of RhB over 5 wt% g-C_3N_4/$CaIn_2S_4$ sample under visible light irradiation；(b) XRD patterns of the 5 wt% g-C_3N_4/$CaIn_2S_4$ sample before and after the cycling photocatalytic experiments.

Fig. 9. Energy band diagram and photocatalytic mechanism of g-C_3N_4/$CaIn_2S_4$ composites.

Fig. 1

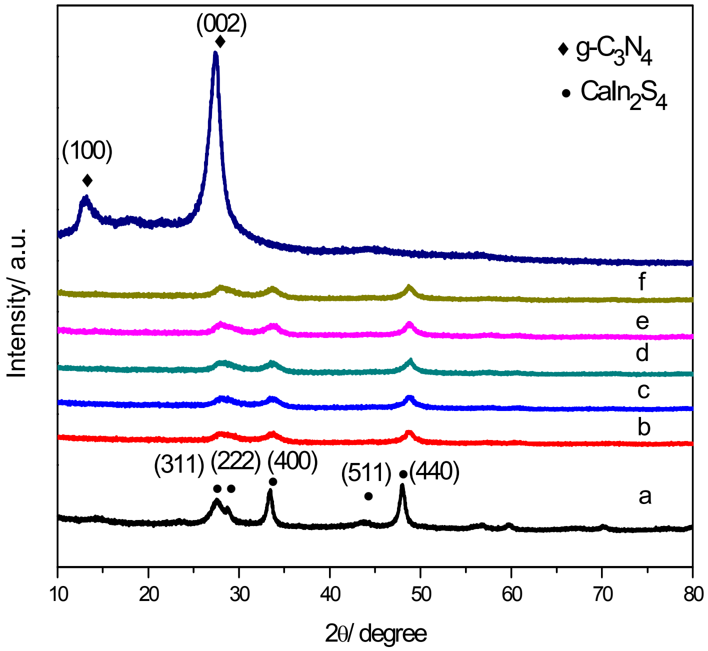
(002)
(100)
♦ g-C_3N_4
• $CaIn_2S_4$
f
e
d
c
b
a
(311) (222) (400)
(511) (440)
Intensity/ a.u.
10 20 30 40 50 60 70 80
2θ/ degree

Fig. 2

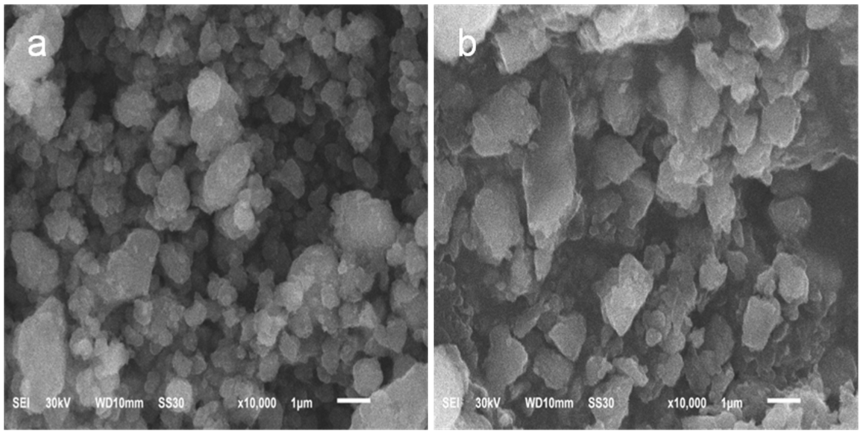
a
b
SEI 30kV WD10mm SS30 x10,000 1μm
SEI 30kV WD10mm SS30 x10,000 1μm

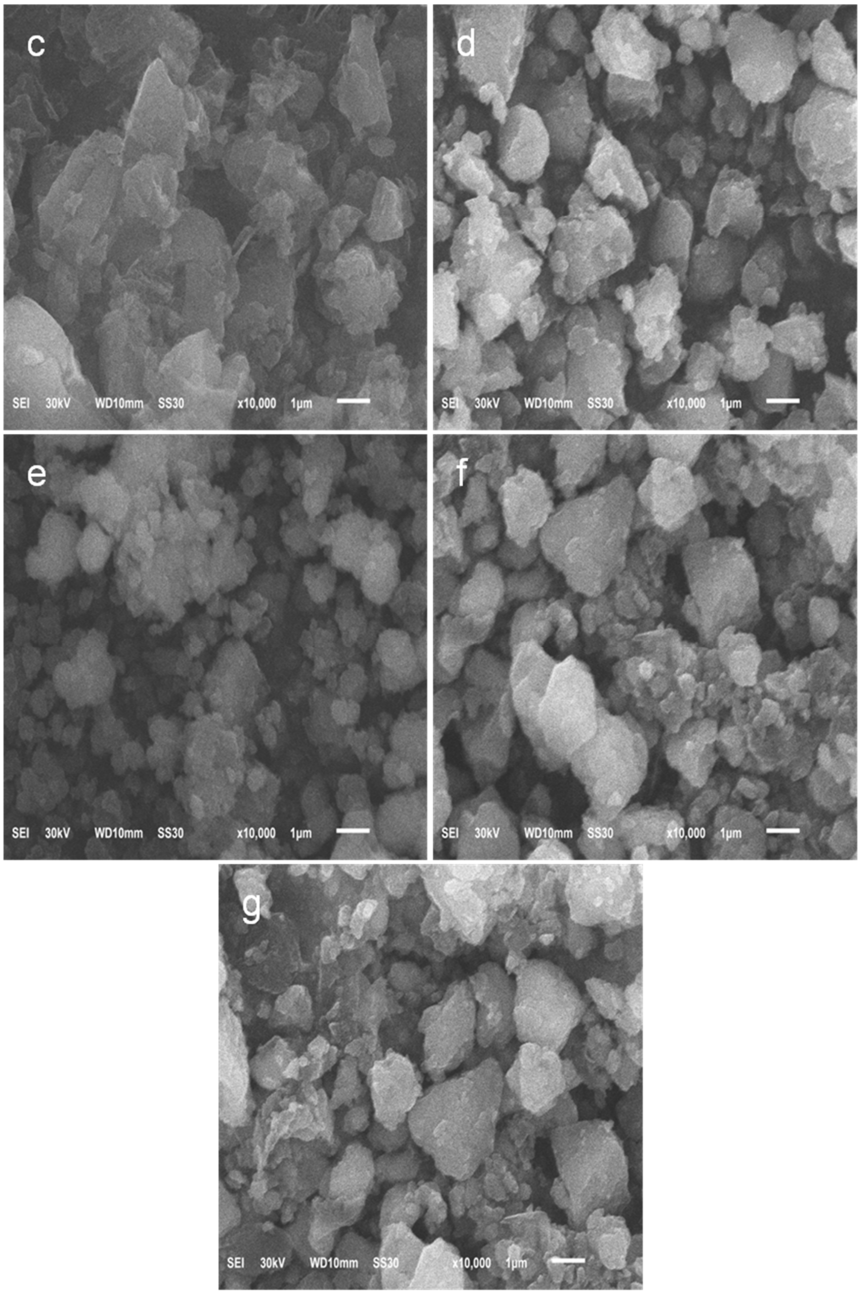
c
SEI 30kV WD10mm SS30 x10,000 1μm
d
SEI 30kV WD10mm SS30 x10,000 1μm
e
SEI 30kV WD10mm SS30 x10,000 1μm
f
SEI 30kV WD10mm SS30 x10,000 1μm
g
SEI 30kV WD10mm SS30 x10,000 1μm

Fig. 3

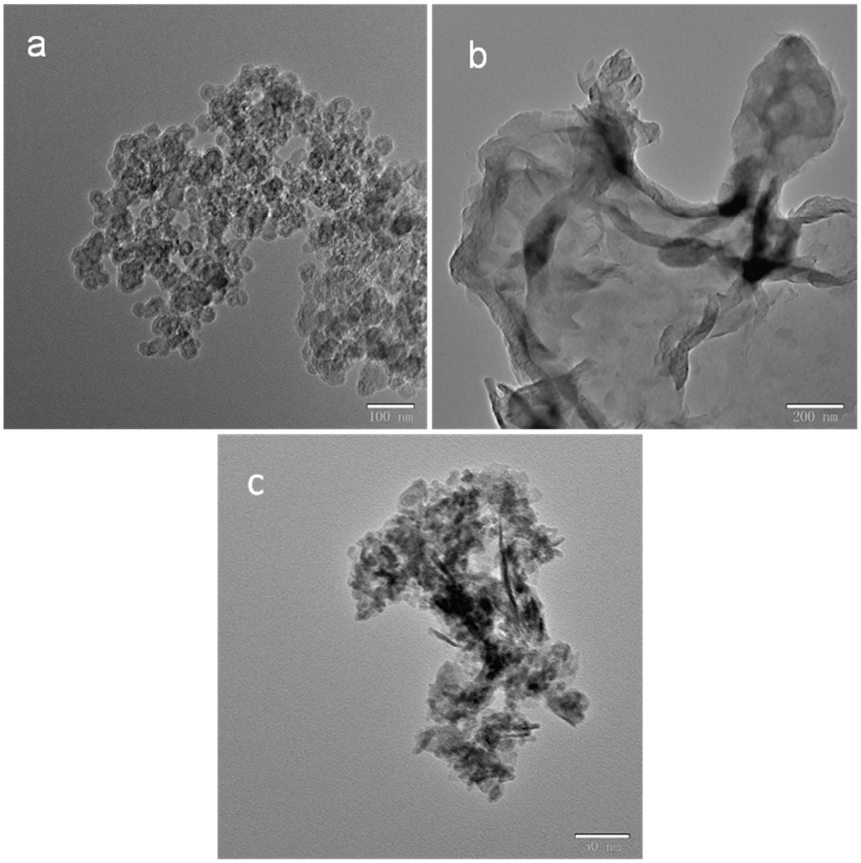
a
100 nm
b
200 nm
c
50 nm

Fig. 4

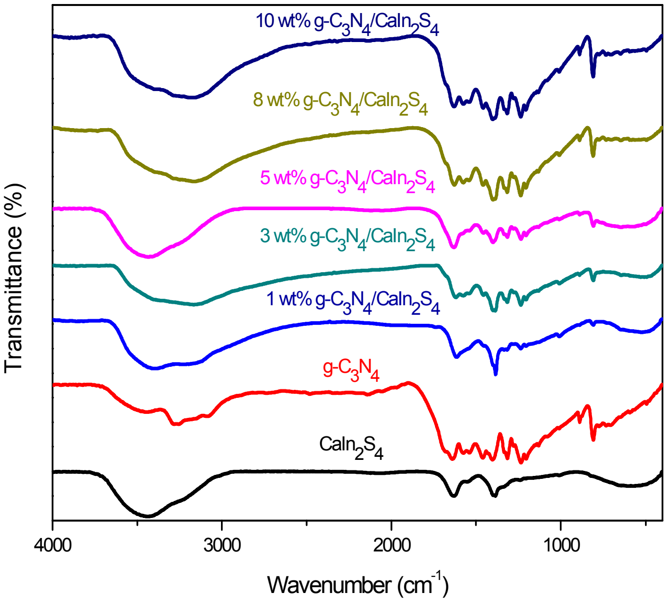
10 wt% g-C_3N_4/$CaIn_2S_4$
8 wt% g-C_3N_4/$CaIn_2S_4$
5 wt% g-C_3N_4/$CaIn_2S_4$
3 wt% g-C_3N_4/$CaIn_2S_4$
1 wt% g-C_3N_4/$CaIn_2S_4$
g-C_3N_4
$CaIn_2S_4$
Transmittance (%)
4000
3000
2000
1000
Wavenumber (cm^{-1})

Fig.5

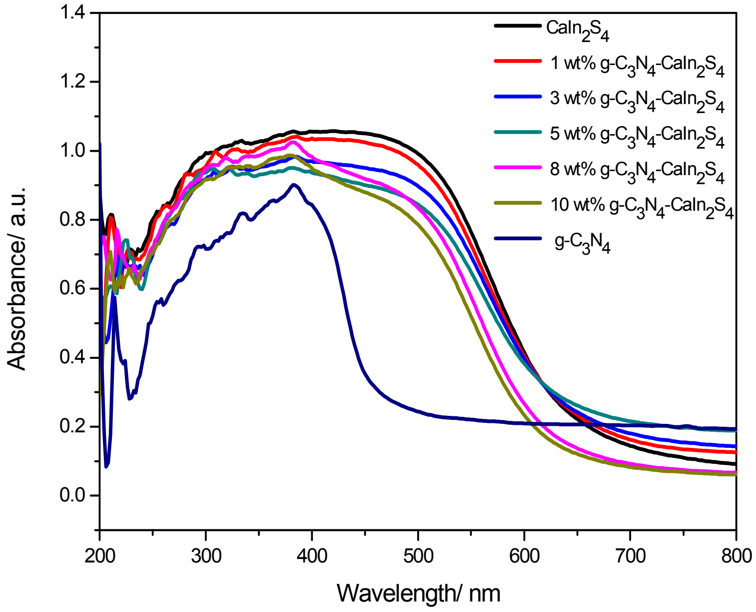
Absorbance/ a.u.
Wavelength/ nm
0.0
0.2
0.4
0.6
0.8
1.0
1.2
1.4
200
300
400
500
600
700
800
CaIn$_2$S$_4$
1 wt% g-C$_3$N$_4$-CaIn$_2$S$_4$
3 wt% g-C$_3$N$_4$-CaIn$_2$S$_4$
5 wt% g-C$_3$N$_4$-CaIn$_2$S$_4$
8 wt% g-C$_3$N$_4$-CaIn$_2$S$_4$
10 wt% g-C$_3$N$_4$-CaIn$_2$S$_4$
g-C$_3$N$_4$

Fig.6

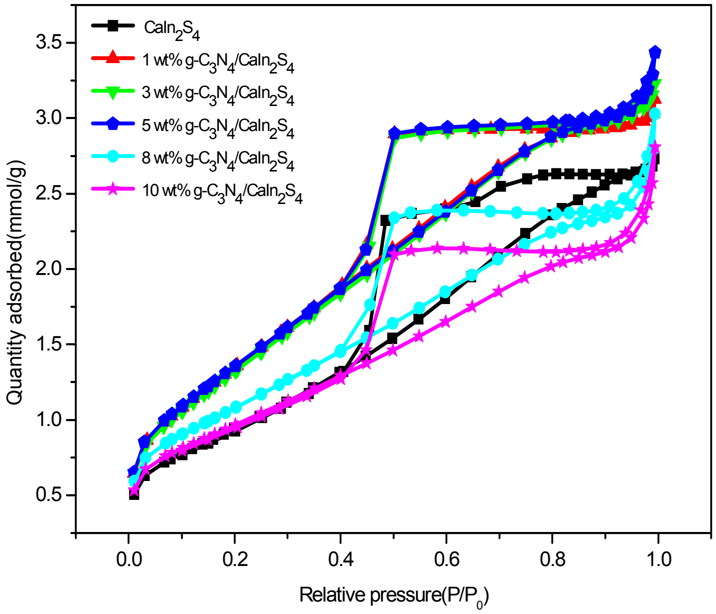
Quantity adsorbed(mmol/g)
Relative pressure(P/P$_0$)
0.5
1.0
1.5
2.0
2.5
3.0
3.5
0.0
0.2
0.4
0.6
0.8
1.0
CaIn$_2$S$_4$
1 wt% g-C$_3$N$_4$/CaIn$_2$S$_4$
3 wt% g-C$_3$N$_4$/CaIn$_2$S$_4$
5 wt% g-C$_3$N$_4$/CaIn$_2$S$_4$
8 wt% g-C$_3$N$_4$/CaIn$_2$S$_4$
10 wt% g-C$_3$N$_4$/CaIn$_2$S$_4$

Fig. 7

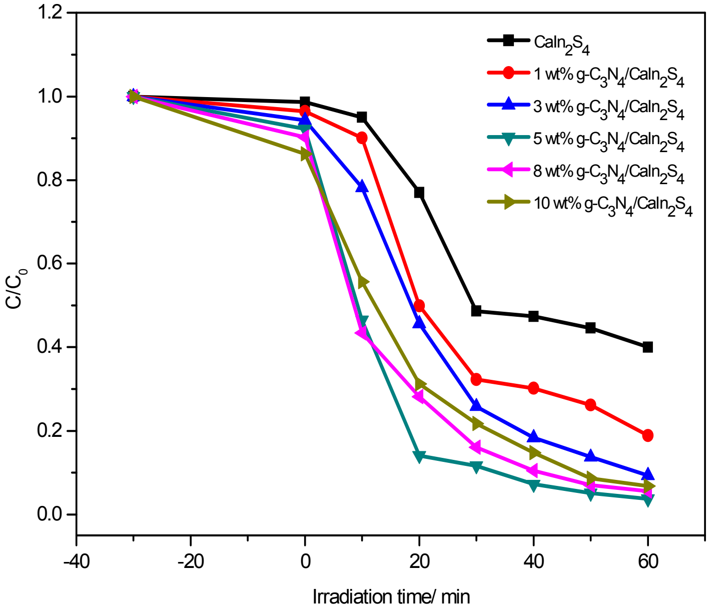
1.2
1.0
0.8
0.6
0.4
0.2
0.0
C/C$_0$
-40
-20
0
20
40
60
Irradiation time/ min
CaIn$_2$S$_4$
1 wt% g-C$_3$N$_4$/CaIn$_2$S$_4$
3 wt% g-C$_3$N$_4$/CaIn$_2$S$_4$
5 wt% g-C$_3$N$_4$/CaIn$_2$S$_4$
8 wt% g-C$_3$N$_4$/CaIn$_2$S$_4$
10 wt% g-C$_3$N$_4$/CaIn$_2$S$_4$

Fig. 8

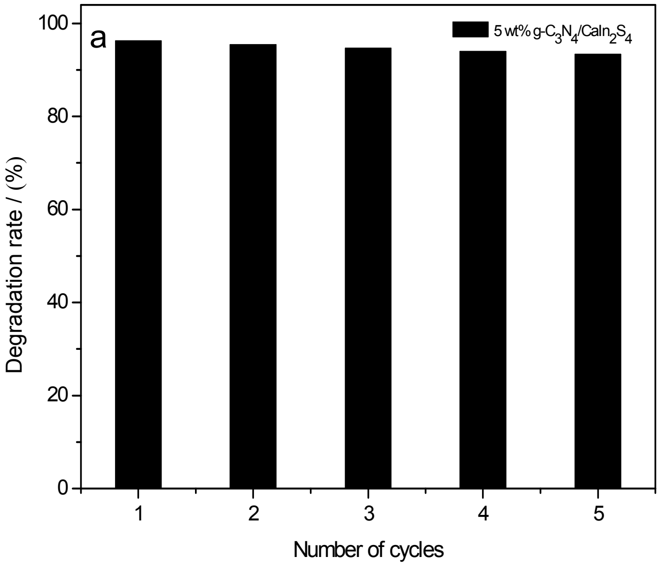
a
5 wt% g-C$_3$N$_4$/CaIn$_2$S$_4$
100
80
60
40
20
0
Degradation rate / (%)
1
2
3
4
5
Number of cycles

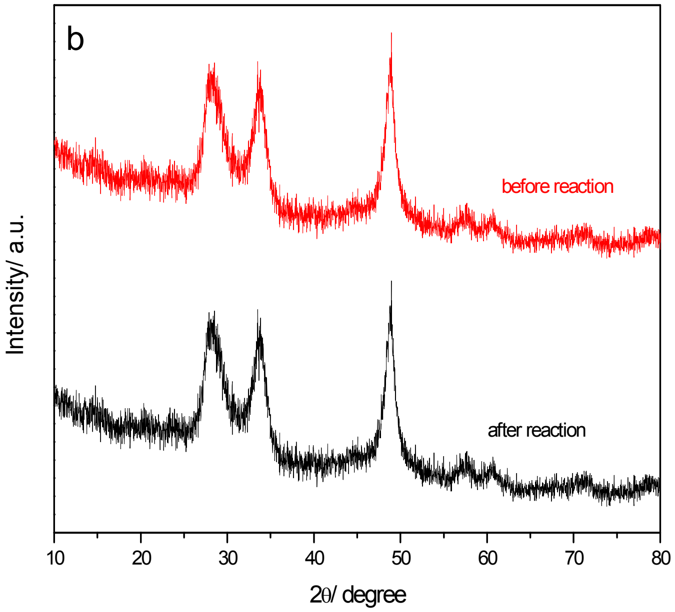
b
before reaction
after reaction
Intensity/ a.u.
2θ/ degree
10
20
30
40
50
60
70
80

Fig. 9

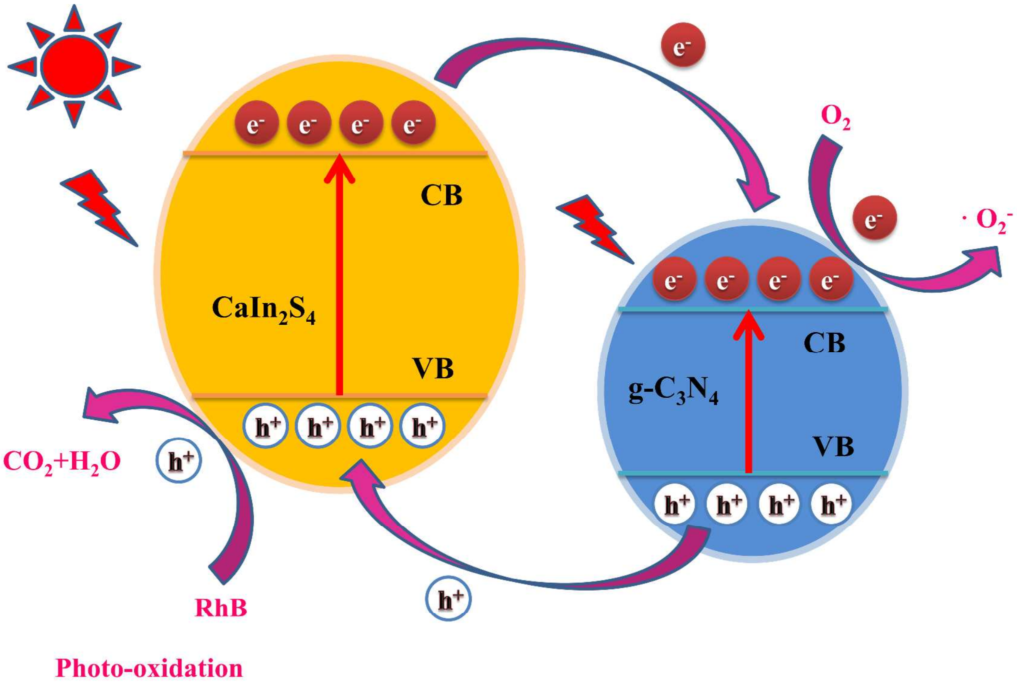
e⁻
e⁻
e⁻
e⁻
e⁻
CB
CaIn₂S₄
VB
h⁺
h⁺
h⁺
h⁺
h⁺
CO₂+H₂O
RhB
Photo-oxidation
O₂
e⁻
· O₂⁻
e⁻
e⁻
e⁻
e⁻
CB
g-C₃N₄
VB
h⁺
h⁺
h⁺
h⁺
h⁺

Table 1. Surface area, pore volume over g-C_3N_4/$CaIn_2S_4$ photocatalysts

sample	g-C_3N_4 (wt %)	S_{BET} (m^2 g^{-1})	pore volume (cm^3 g^{-1})
$CaIn_2S_4$	0	75.1013	0.0929
1% g-C_3N_4/$CaIn_2S_4$	1	113.5364	0.1051
3% g-C_3N_4/$CaIn_2S_4$	3	115.9741	0.1094
5% g-C_3N_4/$CaIn_2S_4$	5	120.6552	0.1140
8% g-C_3N_4/$CaIn_2S_4$	8	88.9464	0.0969
10% g-C_3N_4/$CaIn_2S_4$	10	76.8248	0.0891